Structural-Response Analysis, Fatigue-Life Prediction, and Material Selection for 1 MW Horizontal-Axis Wind-Turbine Blades

M. Grujicic, G. Arakere, E. Subramanian, V. Sellappan, A. Vallejo, and M. Ozen

The problem of mechanical design, performance prediction (e.g., *flap-wise/edge-wise* bending stiffness, fatigue-controlled life, the extent of bending-to-torsion coupling), and material selection for a prototypical 1 MW horizontal-axis wind turbine (HAWT) blade is investigated using various computer-aided engineering tools. For example, a computer program was developed which can automatically generate both a geometrical model and a full finite-element input deck for a given single HAWT-blade with a given airfoil shape, size, and the type and position of the interior load-bearing longitudinal beam/shear-webs. In addition, composite-material laminate lay-up can be specified and varied in order to obtain a best combination of the blade aerodynamic efficiency and longevity. A simple procedure for HAWT-blade material selection is also developed which attempts to identify the optimal material candidates for a given set of functional requirements, longevity and low weight.

1. Introduction

In order to meet the world's ever-increasing energy needs in the presence of continuously depleting fossil-fuel reserves and stricter environmental regulations, various alternative/renewable energy sources are currently being investigated/assessed. Among the various renewable energy sources, wind energy plays a significant role and it is currently the fastest growing installed alternative-energy production technology. In fact, it is anticipated that by 2030, at least 20% of the U.S. energy needs will be met by various onshore and offshore wind-farms (Ref 1). The wind-energy technology is commonly credited with the following two main advantages: (a) there are no raw-material availability limitations; and (b) relative ease and cost-effectiveness of the integration of wind-farms to the existing power grid.

Due to mainly economic reasons (i.e., in order to reduce the electrical energy production cost, typically expressed in $/kW h), commercial wind turbines have grown considerably in size over the last 30 years (Fig. 1). Simply stated, wind speed and, hence, wind-power captured, increases with altitude and this reduces the number of individual turbine units on a wind farm and in turn the cost of operation of the farm. As depicted in Fig. 1, the largest wind turbine unit currently in service is rated at 5 MW and has a rotor diameter of 124 m. As the size of the wind turbines rotor is increasing, the structural and dynamics requirements tend to become more and more challenging to meet and it is not clear what is the ultimate rotor diameter which can be attained with the present material/manufacturing technologies.

Among the main structural/dynamics requirements for wind-turbines are: (a) sufficient strength to withstand highly rare extreme static-loading conditions (e.g., 50-year return-period gust, a short blast of wind); (b) sufficient turbine blade *edge-wise* bending stiffness in order to maintain, at all times, the required minimal clearance between the blade tip and the turbine tower; (c) at least a 20-year fatigue life (corresponds roughly to ca. 10^8 cycles) when subjected to stochastic wind-loading conditions in the presence of thermally fluctuating and environmentally challenging conditions; and (d) various structural/dynamics requirements related to a high mass of the wind-turbine blades (ca. 18 tons in the case of the 62 m long blade). That is not only the blade root and the turbine-hub to which the blades are attached need to sustain the centrifugal and hoop forces accompanying the turning of the rotor, but also the nacelle (i.e., the structure that houses all of the gear boxes and the drive train connecting the hub to the power generator), the tower and the foundations must be able to withstand the whole wind-turbine dynamics. For a more comprehensive overview of the wind-turbine design requirements, the reader is referred to the work of Burton et al. (Ref 2).

Development and construction of highly reliable large rotor-diameter wind turbines is a major challenge since wind turbines are large, flexible, articulated structures subjected to stochastic transient aerodynamic loading conditions. It is, hence, not surprising that several wind-turbine manufacturers face serious problems in meeting the structural-dynamics and fatigue-life turbine-system requirements. The inability to meet the

M. Grujicic, G. Arakere, and **E. Subramanian**, Department of Mechanical Engineering, Clemson University, 241 Engineering Innovation Building, Clemson, SC 29634-0921; and **V. Sellappan, A. Vallejo,** and **M. Ozen**, Ozen Engineering, Inc., 1210 E. Arques Avenue, Suite: 207, Sunnyvale, CA 94085. Contact e-mail: mica.grujicic@ces.clemson.edu.
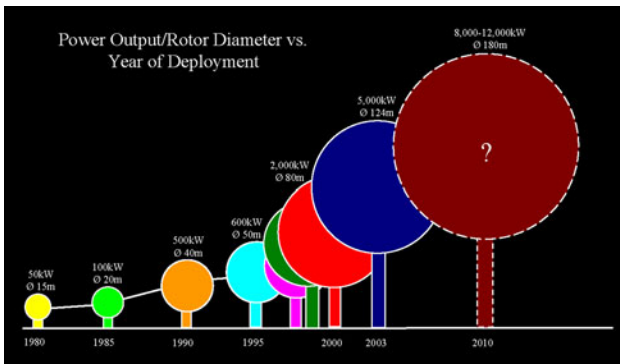
Fig. 1 Variation of the horizontal-axis wind turbine power output and rotor diameter with the year of deployment

Fig. 2 Typical off-shore wind farm. The major wind turbine subsystems are identified

aforementioned requirements is often caused by failure of the transmission gear pinions, failure of bearings, blade fracture, tower buckling, etc. When these problems persist, insurance companies become reluctant in providing their services to the wind-turbine manufacturers causing production shut-down and often company bankruptcy. In order to help prevent these dire consequences, more and more wind-turbine manufacturers are resorting to the use of advanced computer-aided engineering tools, during design, development, verification, and fabrication of their products.

Wind turbine is essentially a converter of wind energy into electrical energy. This energy conversion is based on the principle of having the wind drive a rotor, thereby transferring a power of

$$P = \alpha\beta\rho A v^3 \qquad \text{(Eq 1)}$$

to the electrical generator, where α is an aerodynamic efficiency parameter, β is a drive-train efficiency parameter; ρ is air density, A rotor surface area, and v the wind speed. The P/A ratio is commonly referred to as the *specific power rating*. To attain rotor rotation and a high value of α, the rotor has to be constructed as a set of three (sometime two) aerodynamically shaped blades. The blades are (typically) attached to a horizontal hub (which is connected to the rotor of the electrical generator, via a gearbox/drive-train system, housed within the nacelle). The rotor/hub/nacelle assembly is placed on a tower and the resulting wind-energy converter is referred to as the horizontal-axis wind turbine (HAWT). A photograph of an offshore wind turbine is provided in Fig. 2. All major components of the turbine are labeled for identification.

Turbine blades are perhaps the most critical components in the present designs of wind turbines. There are two major designs of the wind-turbine blades: (a) the so-called *one-piece* construction (Fig. 3a and b) and the so-called *two-piece* construction (Fig 3b). In both cases, the aerodynamic shape of the blade is obtained through the use of separately fabricated and adhesively joined outer-shells (often referred to as the *outer skin* or the upper and lower *cambers*). The two constructions differ with respect to the design and joining of their load-bearing interior structure (running down the blade length). In the case of the one-piece construction, the supporting structure consists of a single close box spar which is adhesively joined to the lower and upper outer shells. Since the stresses being transferred between the outer shells and the spar are lower in
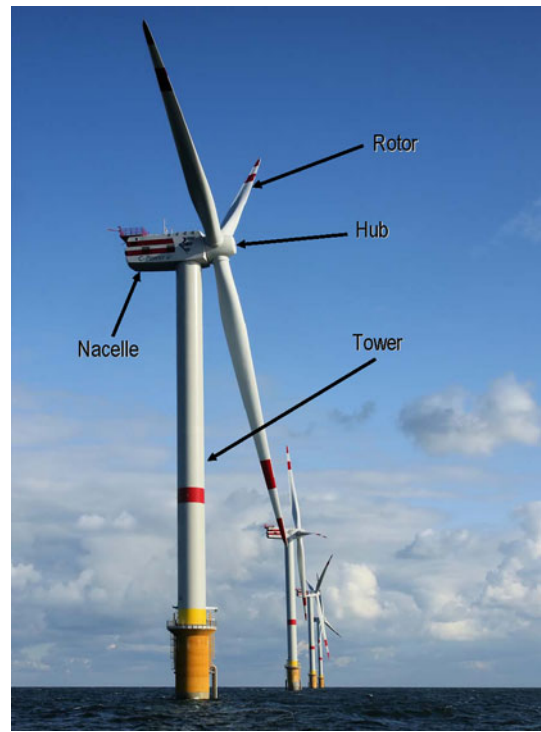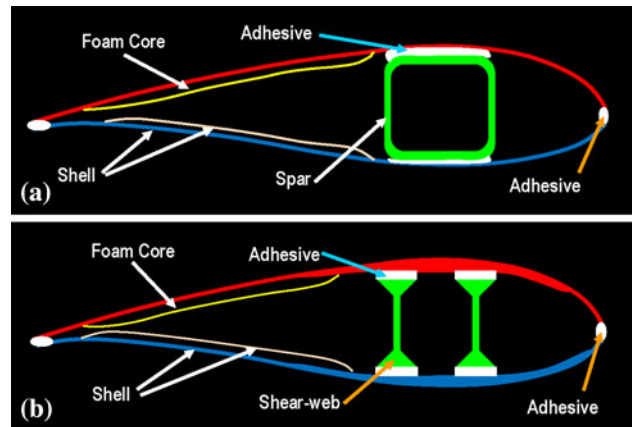

Fig. 3 Typical turbine-blade cross-sectional area in the case of: (a) the one-piece construction; and (b) the two-piece construction

magnitude, a lower-strength adhesive like polyurethane is typically used. In the case of the two-piece construction, the supporting structure consists of two stiffeners/shear-webs which are also adhesively joined with the outer shells. However, since the adhesive joints have to transfer the stresses between the two stiffeners in addition to transferring stresses between the outer shells and the shear webs, higher-strength adhesives like epoxy have to be used.

The main objective of this work is to help further advance the use of computer-aided engineering methods and tools (e.g., geometrical modeling, structural analysis including fatigue-controlled life cycle prediction and material-selection

methodologies) to the field of design and development of HAWT-blades. Consequently, many critical decisions regarding the design and fabrication of these components can be made in the earlier stages of the overall design cycle. This strategy has been proved to yield very attractive economic benefits in the case of more mature industries such as the automotive and the aerospace industries.

Specific issues addressed in this work include the problem of automated generation of a geometrical model and a full finite-element input deck, coupled with realistic wind-induced loading conditions for a given set of HAWT-blade geometrical, structural and material parameters. Also, the use of a computer-aided material-selection methodology for identification of the optimal HAWT-blade materials for a given set of functional, longevity, and cost-efficiency requirements is considered.

The organization of the paper is as follows. A brief overview of the approach used for automated HAWD-blade geometrical model and the full finite-element input deck generation is presented in Section 2.1. The quasi-static finite-element procedure and a post-processing methodology used, respectively, to quantify the key blade structural-performance parameters and the blade fatigue life are described in Sections 2.2 and 2.3. A single HAWT-blade material-selection procedure is presented in Section 2.4. The results are obtained and discussed in Section 3. A brief summary of the work carried out and the results obtained is presented in Section 4.

2. Computational Procedures

2.1 Geometrical and Meshed Models

As mentioned earlier, the subject of the present investigation is a structural-response analysis, durability assessment/prediction, and material selection for a single prototypical 1 MW HAWT-blade. The wind-turbine blade is essentially a cantilever beam mounted on a rotating hub. The aerodynamic shape of the blade is formed by relatively thin outer shells. The loads acting on the blade are mainly supported by a longitudinal box-shaped spar or by a pair of the C-shaped shear webs. To reduce the bending moments in blade section away from the blade root (the section where the blade is attached to the hub), wind-turbine blades are generally tapered. Tapering typically includes not only the blade cross section, but also the shell/beam/web thickness. This ensures that different blade sections experience comparable extreme loading (e.g., the maximum strain). In addition to the taper, turbine blade generally possess a certain amount of twist along their length. Twist is beneficial with respect to self-starting of the rotor and through the bending/torsion coupling effects help improve wind-power capture efficiency.

To create a prototypical wind-turbine blade, a computer program was first developed which can generate one of the standard airfoil profiles such as the *Wortmann FX84W*, the *Althaus AH93W*, or the *NACA-23012* (e.g., Ref 3) of the given dimensions. The program is implemented in MATLAB, a general-purpose mathematical package (Ref 4). Next, the program further enables the creation of the entire wind-turbine blade geometrical model (in the *.stl* format) and a finite-element mesh model (for a given set of parameters related to the taper, twist, shear-web lateral positions, mesh-topology, etc.).

An example of the wind-turbine blade geometrical model and of the corresponding finite-element meshed model are displayed, respectively, in Fig. 4(a) and (b). The case of a
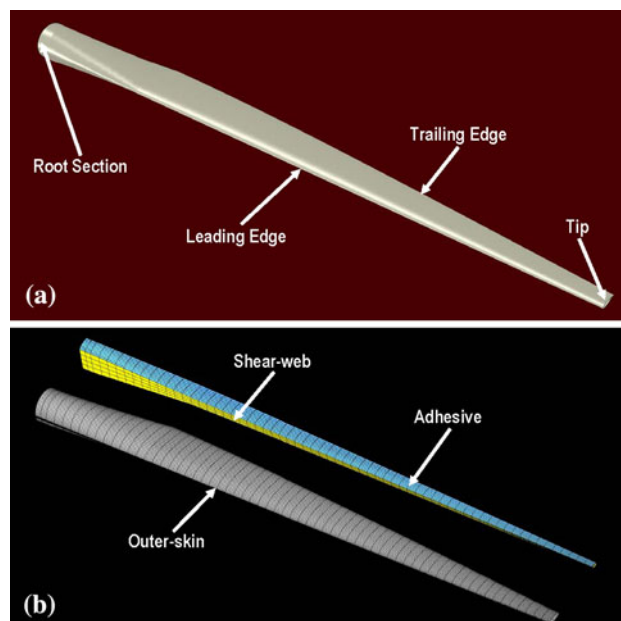

Fig. 4 Typical: (a) geometrical and (b) meshed models of a single wind-turbine blade analyzed in this work

prototypical 1 MW wind-turbine with a 0.44 kW/m² specific power rating (a ratio of the power rating to the rotor swept area) was considered in this work. Following the HAWT-blade design procedure outlined in Ref. 5, a series of HAWT-blades with the following general dimensions and geometrical parameters was constructed and analyzed: length = 30 m, blade diameter at the root = 1.5 m, chord length at the first airfoil station located at 25% from the root = 2.1 m, chord length at the blade tip = 0.67 m (with a linear taper in-between), S818 airfoil shape, and a total twist angle = 10.5°. Also, typically, the two outer skins and the two webs are meshed using ca. 4,160 and ca. 512 first-order four-node composite-shell elements, respectively, while the two thick layers of adhesives which connect the webs to the outer shells, were meshed using ca. 1,088 first-order eight-node hexahedral solid elements. To facilitate optimization of the HAWT-blade composite-laminate lay-up, all the meshes used were of a structured character.

The geometry/mesh generator program described above enabled an automated generation of the entire finite-element input deck for a selected set of parameters which is a critical requirement for computer-efficient design-of-experiments and design-optimization analyses. For example, lateral/transverse locations of the two shear webs and the thicknesses of two spar-caps (horizontal beam-sections bridging the shear webs) and two adhesive layers could be readily varied.

2.2 Wind-Turbine Blade Structural Analysis

Wind-turbine blades are generally oriented in such a way that their wide faces are roughly parallel with the hub-rotation axis and, in the case of the so-called *up-wind design*, with their leading edge facing the wind. In other words, the effective wind direction as experienced by the blades is in the rotational plane of the rotor although the real-wind direction is orthogonal to it. Furthermore, due to the aerodynamic shape of the blades, significant lift-induced torque is produced causing the rotor to spin.

Lift-type wind-based loads described above not only cause rotor to spin, but also lead to the so-called *flap-wise* bending of the blades. It should be recognized that the lift-induced loading has both a persistent/static-like and a time-varying component (the latter one is due to natural variability of the wind). In addition, the relative fraction of the two load components changes during rotation of the rotor due to the so-called *wind-shear* effects (i.e., due to a natural increase in the wind speed with an increase in the height above the terrain).

In addition to the lift-related loads discussed above, wind-turbine blades are also subjected to gravity loads. These loads are the highest in magnitude when the blade is in a nearly horizontal position and they cause edge-wise bending of the wind-turbine blade. Since, the blades bend one way when they are on the right-hand side of the tower while they bend in the other direction when they are on the left-hand side of the tower; gravity loading also contains a variable component.

Wind-turbine blades are also subjected to centrifugal loading due to rotation of the rotor. Nevertheless, since the upper-bound angular velocity of the rotor is typically in a 10-20 rpm range, centrifugal-tensile loads along the blade length are generally not considered as design-controlling/life-limiting loads (and are, hence, ignored in this work).

To account for the typical wind-turbine blade loading discussed above, a series of two-dimensional aerodynamic analyses was carried out using the *Javafoil* computer program (Ref 6). This program solves the flow equations over an airfoil by implementing the boundary integral method. For the given airfoil profile and size, the wind speed and the angle of attack, the program generates a distribution of pressures over the blade surface. An example of the results pertaining to the spatial distribution of the coefficient of pressure (a ratio of the pressure minus mean-stream pressure difference and the half product of mean-stream air-density and squared wind velocity) is displayed in Fig. 5. These analyses are repeated for up to 10 equally spaced wind-turbine blade cross sections. The results obtained were then used within an interpolation algorithm to compute pressure distribution over the entire blade surface.

Two wind-induced loading conditions were considered:

(a) For the structural-response analysis, peak loads were derived by considering a 50-year extreme gust of 70 m/s (IEC Class 1 (Ref 7). The blade is assumed to be i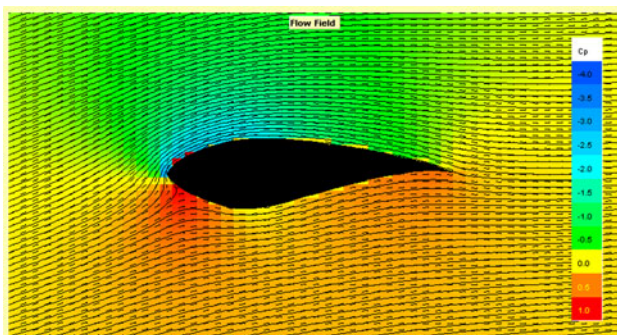n a fully *feathered* position (i.e., pitch of the blade is adjusted to obtain the wind attack-angle associated with the lowest aerodynamic loads) with a $\pm 15°$ variation in wind direction. To attain the most conservative loading case, it was assumed that the gust-induced loading results in each blade section simultaneously reaching its local maximum-lift coefficient condition; and

(b) For the fatigue-life prediction/assessment analysis, loading was determined using the average wind speed at the wind-turbine power rating. This velocity was computed using the procedure outlined in Ref 5. Within this procedure, the specific power rating (taken to be 0.44 kW/m^2) is defined as a product of rotor efficiency coefficient ($\alpha = 0.5$), a drive-train efficiency ($\beta = 0.925$), air density ($=1.225$ kg/m^3), and the third power of the wind rated speed ($=130\%$ of the wind mean speed at the rotor hub elevation). This procedure yielded a wind mean speed at the hub elevation of 7.67 m/s in the direction of rotor axis. It should be also noted that this procedure enabled determination of the mean-level wind-induced loads in the HAWT-blade. To account for the time-varying component of the wind-induced and gravity loading, the so-called *WISPER* (wind spectrum reference) loading history/profile (Ref 8) (a reference load spectrum typically used in the design of wind-turbine blades in Europe) was used (after proper scaling).

To determine the quasi-static structural response of the blade, a static finite-element analysis was carried out in which the root-edge of the blade was fixed and the blade outer surfaces subjected to the aforementioned gust-induced loading. The results of these analyses were used to determine the turbine-blade bending stiffness (as quantified by the average displacement of its tip section) and by the blade strength (as measured by the largest value of the von Mises equivalent stress within its interior) as well as the extent of bending-to-torsion coupling (as measured by the loading-induced twist at the blade tip). In addition due to the fact that wind-induced loading was found to be nearly proportional (i.e., the orientation of the in-plane principal coordinates system over the most highly stress blade-surface sections was found not to change significantly during loading), the results of the structural analysis were used also in the fatigue-life assessment analysis (discussed in next section). In other words, local stresses are assumed to scale linearly with the level of local wind-induced loading so that the gust-based stresses can be used to directly calculate the corresponding stresses at any level of wind-induced loading.

All the calculations pertaining to the structural response of the wind-turbine blade were done using ABAQUS/Standard, a commercially available general-purpose finite-element program (Ref 9).

2.3 Wind-Turbine Blade Fatigue-Life Prediction

It is well-established that in most cases, the life cycle of a wind-turbine blade is controlled by its fatigue strength (in the presence of local thermal and aggressive environmental conditions). While it is generally fairly straight forward to quantify fatigue strength of the structural materials (glass- or carbon-fiber reinforced polymer-matrix composites, in the case of wind-turbine blades) under constant-amplitude loading conditions, relating the material fatigue strength to the component (a turbine blade, in the present case) is a quite challenging task.

Fig. 5 An example of the results pertaining to the two-dimensional distribution of the coefficient of pressure and the streamlines in the region surrounding the airfoil for the case of a 10° angle of attack (the angle between the wind direction and the airfoil chord.)

This is primarily due to the fact that time-varying loading (e.g., WISPER) is associated with nonconstant amplitude. In other words, real time-varying wind-induced loading is irregular and stochastic, and the associated load history affects the component fatigue life in complex ways. The procedure used in this work to correlate the material fatigue strength with the component fatigue strength/life is based on the use of a cycle-counting algorithm (the so-called *Rainflow* cycle-counting analysis; Ref 10), a linearized Goodman diagram (e.g., Ref 11) to account for the effect of mean-stress/strain on the material fatigue life/strength and the Miner's linear-superposition principle/rule (Ref 12). The rainflow analysis, the Goodman diagram, and the Miner's rule are briefly overviewed in the remainder of this section.

2.3.1 Rainflow Analysis. When a time-varying load signal is recorded over a sampling period, and needs to be described in terms of a three-dimensional histogram (each bin of which being characterized by a range of the signal amplitude and a range of the signal mean-value), procedures like the rainflow counting algorithm are used. Within this procedure, the first step involves converting the original load signal into a sequence of load peaks and valleys. Then, the cycle-counting algorithm is invoked. To help explain the rainflow cycle-counting algorithm, a simple load signal (after the peak/valley reconstruction) is depicted in Fig. 6(a), with the time axis running downward.
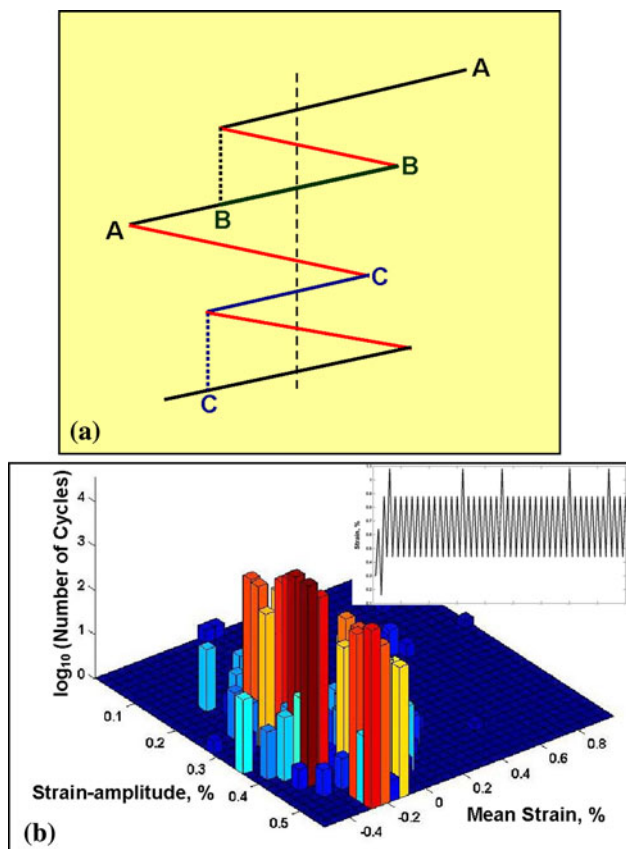
Within the rainflow cycle-counting algorithm, separate counting of load half-cycles is carried out for the ones starting from the peaks and the ones starting from the valleys. In Fig. 6(a), only the half-cycles originating from the peaks are analyzed. A half-cycle then starts from each peak and ends when one of the following three criteria is met:

(a) when the end of the signal is reached (Case A in Fig. 6a);
(b) when the half-cycle in question runs into a half-cycle which originated earlier and which is associated with a higher peak value (Case B in Fig. 6a); and
(c) when the half-cycle in question runs into another half-cycle which originated at a later time and which is associated with a higher value of the peak (Case C in Fig. 6a).

Once all the half-cycles are identified they are placed in bins, each bin being characterized by a range of the load amplitude and the load mean-value. An example of the resulting three-dimensional histogram showing the number of cycles/half-cycles present in the load signal associated with a given combination of the load amplitude and the load mean-value is depicted in Fig. 6(b).

2.3.2 Goodman Diagram. Before presenting the basics of the Goodman diagram, it is important to recognize that fatigue life of a material is a function of both the stress/strain amplitude and the stress/strain mean-value. Often, the stress/strain mean-values are quantified in terms of an R-ratio which is a ratio of the algebraically minimum and the algebraically maximum stress/strain values (associated with the constant-amplitude cyclic-loading tests). From the definition of the mean stress/strain, it can be readily shown that fatigue-loading tests carried out under constant R-ratio conditions, correspond to the tests in which the mean stress/strain scales with the corresponding amplitude. To construct the Goodman diagram, constant-R/constant-amplitude fatigue-test results are plotted, in a stress/strain amplitude versus stress/strain mean-value diagram. As depicted, in Fig. 7, constant-R data fall onto a line
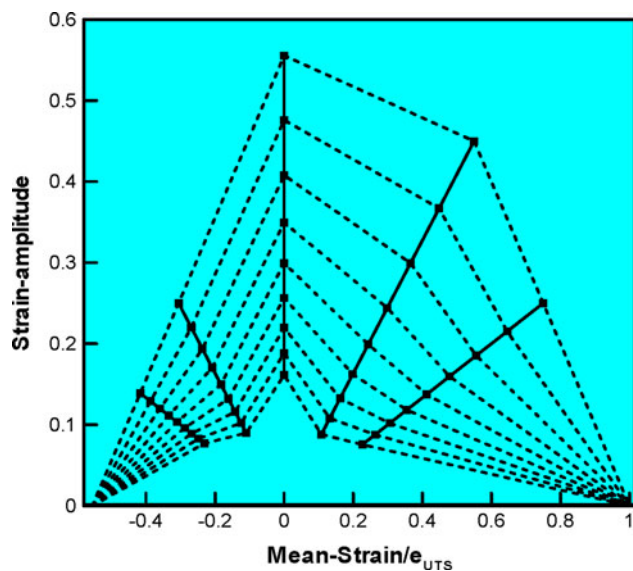

Fig. 6 (a) Application of the rainflow cycle-counting algorithm to a simple load signal after the peak/valley reconstruction. Lease see text for explanation; and (b) the resulting three-dimensional histogram showing the number of cycles/half-cycles in each mean stress/strain-stress/strain amplitude bin

Fig. 7 An example of the Goodman diagram showing constant fatigue-life data (*dashed lines*) and constant R-ratio data (the *solid lines* emanating from the origin)

emanating from the origin. In Fig. 7, $R = 0.1$ and $R = 0.5$ data are associated with a positive/tensile mean stress/strain value, $R = -1$ corresponds to a zero mean-value, while $R = 10$ and $R = 2$ pertain to a negative/compressive mean-value.

To construct the corresponding linearized Goodman diagram, constant fatigue-life data associated with different R-ratio values are connected using straight lines. To complete the construction of the Goodman diagram, the constant fatigue-life lines are connected to the ultimate tensile stress/strain and to the ultimate compressive stress/strain points located on the zero-amplitude horizontal axis. The completed Goodman diagram displayed in Fig. 7 then enables, through interpolation, determination of the fatigue life for any combination of the stress/strain amplitude and stress/strain mean-value. Hence, a three-dimensional histogram similar to that one shown in Fig. 6(b) can be constructed except that the number of cycles here represents the total number of cycles to failure rather than the number of cycles in the analyzed load signal. An example of such three-dimensional histogram is displayed in Fig. 8.

2.3.3 Miner's Rule. The cycle-counting procedure described earlier enables computation of the number of cycles/half-cycles in the given load signal which fall into bins of a three-dimensional histogram (Fig. 6b). The use of the Goodman diagram, on the other hand, enables the computation of a similar tri-dimensional histogram but for the number of cycles to failure (i.e., the fatigue life, Fig. 8). According to the Miner's rule, a ratio of the number of cycles and the corresponding total number of cycles, for a given combination of the stress/strain amplitude and stress/strain mean-value, defines a fractional damage associated with this component of the loading. The total damage is then obtained by summing the fractional damages over all combinations of the stress/strain amplitude and the stress/strain mean-value.

The total fatigue life under the given nonconstant amplitude time-varying loading is obtained by dividing the load-signal duration by the total fractional damage. This procedure clearly postulates that fatigue failure corresponds to the condition when the total damage is equal to unity.

2.4 Wind-Turbine Blade Material Selection

From simple consideration of basic functional and longevity requirements for a HAWT-blade, it can be readily concluded
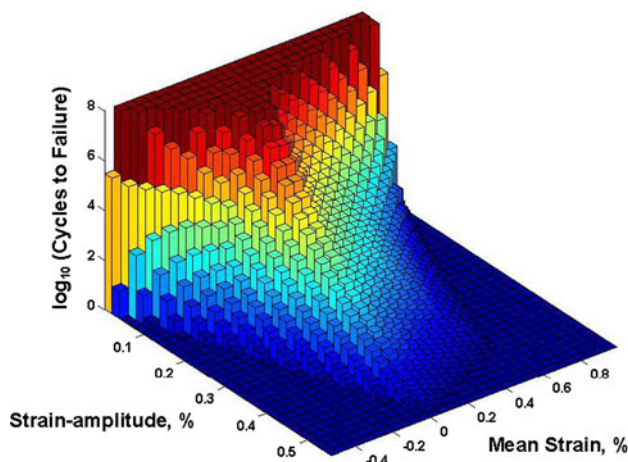

Fig. 8 An example of the three-dimensional histogram showing the effect of stress/strain amplitude and the stress/strain mean-value of the material fatigue life

that the main blade material-selection indices must be based on the following material properties:

(a) a high material stiffness to ensure retention of the optimal aero-dynamic shape by the blade while subjected to strong-wind loading conditions;

(b) a low mass density to minimize gravity-based loading; and

(c) a large high-cycle fatigue strength to ensure the required 20-year life cycle with high reliability.

As mentioned earlier, the HAWT-blade is essentially a cantilever beam. If the material-selection methodology proposed by Ashby (Ref 13) is utilized, then the first material-selection index can be defined by requiring that the blade attains a minimal mass while meeting the specified bending-stiffness requirements (or alternatively that the blade attains maximum bending stiffness at a given mass level). Since the blade mass scales directly with its average cross-sectional area while its, stiffness scales roughly with the square of its, cross-sectional area, following Ashby's material-selection procedure one can readily derive the following "*light, stiff beam*" material-selection index:

$$M_1 = E^{1/2}/\rho \qquad \text{(Eq 2)}$$

where E is the materials Young's modulus and ρ is its density.

The use of M_1 in the HAWT-blade material selection would normally identify foam-like materials as potential candidates. In these materials, their low stiffness (as quantified by the value of their Young's modulus, E) is more than compensated by their low ρ value. Consequently, M_1 takes on a large value in the case of foam materials suggesting their suitability for use in the HAWT-blade applications. However, foam materials would yield very bulky blades which could present serious design, manufacturing, installation and operational problems. In addition, potentially open-cell structure and the associated high water-permeability/moisture-absorption can disqualify these materials from being used in the HAWT-blade applications. To overcome these problems, a second material-selection index (more precisely, a lower-bound material-property limit) is proposed which requires that the HAWT-blade materials possess a minimal level of absolute stiffness, i.e.,

$$M_2 \geq E. \qquad \text{(Eq 3)}$$

Typically, the minimal level of the Young's modulus required for a given-blade material is in a 15-20 GPa range.

The two material-selection indices defined above utilize two (E and ρ) out of the three previously identified material properties. Inclusion of the third material property (the fatigue strength) into a material-selection index is, however, quite challenging. The reason is that, as discussed in the previous section while the constant-amplitude fatigue strength associated with a given load mean-value and a given fatigue life can be readily determined, HAWT-blade material selection requires the use of a variable-amplitude fatigue life.

As demonstrated in the previous section, the variable-amplitude fatigue life can be, in principle, computed for a given combination of the sustained quasi-static and time-varying loads. However, the procedure which is used in this calculation also entails the knowledge of the constant-amplitude fatigue data under different mean-value/R-ratio conditions. Since the

generation of such data requires an extensive set of experimental tests, these data are not always available (in particular, in the open literature). Hence, the HAWT-blade material-selection procedure used in the present work had to rely on more readily available material properties. Specifically, the *endurance limit* [i.e., the infinite-life constant-amplitude fatigue strength (under a zero mean loading, i.e., $R = -1$)] will be used in the HAWT-blade material selection. Since materials with higher fracture toughness will fail in a more gradual manner (enabling a longer life of the blade between the time of initiation of the first cracks to the final failure). In this way, blades which have suffered fatigue-induced damage can be identified during periodic inspections and replaced, preventing more serious consequences, which may result from their unexpected catastrophic failure while in service.

Based on the discussion presented above, the third and the final HAWT-blade material-selection index can be defined as:

$$M_3 = \sigma_{\text{end}} \cdot G_{\text{Ic}}, \tag{Eq 4}$$

where σ_{end} is the endurance limit and G_{Ic} the mode-I fracture toughness.

Clearly, the higher is the value of each of the three aforementioned material indices, the more suited is a given material for use in the HAWT-blade applications.

3. Results and Discussion

As discussed in Section 2, as part of this work, a computer program was developed which enables automated creation of fully parameterized geometrical and meshed models, as well as the generation of a complete finite-element input deck for a large single composite-laminate 1 MW HAWT-blade. For a given choice of the airfoil shape, down-the-length taper and blade twist-angle, the program enables the user to specify lateral location of the shear webs, thickness for all aerodynamic (i.e., the outer skins) and structural (i.e., the shear webs, the spar caps, the adhesive layers) component thicknesses and composite-laminate ply stacking for each component as a whole or for different portions of the same component. In addition, interfacing of the model-generation computer program with an aerodynamics analysis computer program (Ref 6) enabled automated generation of the sustained wind-based loading conditions. This was complimented by the addition of nonconstant amplitude reference time-varying loading to construct fairly realistic in-service loading conditions experienced by a large composite-laminate HAWT-blade. The results obtained from the quasi-static finite-element analyses of the HAWT-blade enabled not only investigation of the structural response of the blade (i.e., the extent of the blade tip deflection, the extent of blade-tip rotation due to bending-to-torsion coupling aero-elastic effects, etc.), but also predictions of the HAWT-blade high-cycle fatigue-controlled life cycle.

Due to space limitations, only few representative results obtained in the present investigation will be shown and discussed in the following sections. This will be followed by a presentation of the results pertaining to the HAWT-blade material selection.

It should be noted that each portion of this work included a mesh-convergence study to ensure that the finite-element mesh used was a good compromise between a computational accuracy and computational cost. The results of the mesh-convergence studies will not be shown for brevity.

3.1 The Baseline Case

At the beginning of the present investigation, a baseline case was first established/constructed which is representative of the current commercial 1 MW HAWT-blade designs. In the baseline case which is based on the S818 airfoil shape (Ref 14), Fig. 9(a), the primary structural member is a box-shape spar with (vertical) shear webs being located at distances equal to 15% and 50% of the section-chord length (as measured from the leading edge) and a substantial build-up in the spar cap thickness between the two vertical shear-webs. Examination of the HAWT-blade construction depicted in Fig. 9(a) suggests that due to a relatively large spar-cap width and laminate thickness, good edge-wise bending stiffness/strength is expected. This is, however, attained at the expense of the flat-wise bending stiffness/strength which could have been increased should the shaft portion of the shear web had been placed in the section of the blade associated with the largest blade thickness.

A typical planform, Fig. 9(b), is assigned to the blade. The plan-form shows the variation of the blade chord-length with a radial distance r from the hub-rotation axis with R being the radial location of the blade tip. Figure 9(b) shows that there is a linear taper from the maximum-chord section located at $r/R = 0.25$ to the blade tip ($r/R = 1.0$). The blade root is located at $r/R = 0.05$ and is circular in cross section. The cross section is assumed to remain circular up to $r/R = 0.07$ and thereafter undergoes a gradual transition to the pure airfoil section located at $r/R = 0.25$.

As mentioned earlier, HAWT-blades are commonly twisted. Consequently, the baseline-blade case analyzed here was given a twist along its length. Specifically, the airfoil sections located at $r/R = 0.25$, 0.5, 0.75, and 1.0 were twisted by 10°, 2.5°, 0°, and $-0.5°$, respectively.
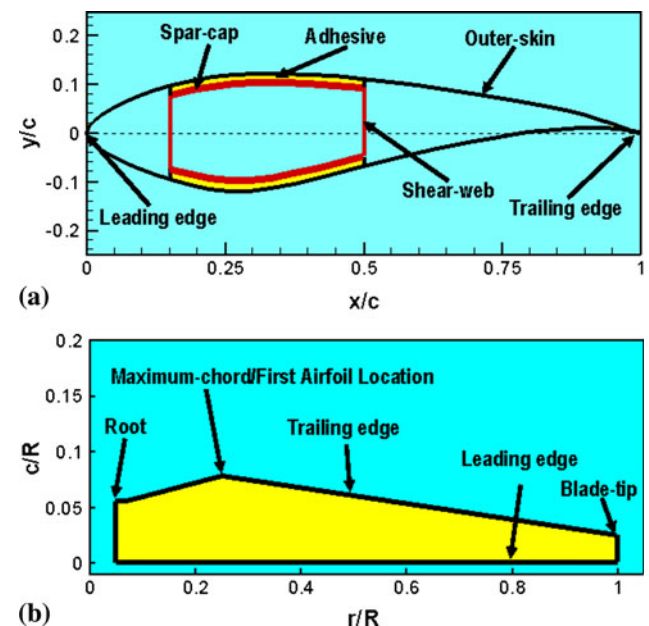

Fig. 9 Baseline case of the HAWT-blade analyzed in this work: (a) the airfoil cross section; and (b) the planform

The exterior airfoil skins and the interior vertical shear webs are constructed using a sandwich-like material consisting of (−45°/0°/45°) tri-axial fiber-glass composite-laminate face-sheets separated by a balsa-wood core. The spar caps are constructed of alternating equal-thickness layers of the tri-axial laminates (described above) and unidirectional laminates making the contribution of 0° laminate and the off-axis laminate 70% and 30%, respectively. A summary of the composite-laminate lay-up sequences and ply thicknesses used in different sections of the baseline HAWT-blade design is provided in Table 1.

As mentioned earlier, all composite laminates mentioned above were based on epoxy matrix reinforced with E-glass fibers. As far as the adhesive layers connecting the spar caps to the interior faces of the skins are concerned, they were taken to be epoxy based. A summary of the stiffness, mass, and composite mixture properties (where applicable) of the materials used are provided in Table 2. In Table 2, *Tri*, *Uni*, and *Mix* are used to denote, respectively, the tri-axial, uni-axial, and the spar-cap mixture composite laminates.

3.1.1 Structural Response of the Baseline HAWT-Blade. A set of examples of the results pertaining to the structural responses of the baseline HAWT-blade is displayed in Fig. 10(a), 11, 12(a), and 13. These results pertain to the case when the blade is in the horizontal position; it is fixed at its root and subjected to the gravity loading, centrifugal forces along its length and the aerodynamic forces resulting from pressure difference across the blade thickness under the gust-based loads.

In Fig. 10(a), a spatial-distribution plot of the baseline HAWT-blade external-skin displacement magnitudes is displayed. The results displayed in this figure reflect mainly the intrinsic edge-wise bending stiffness of the blade which is important for the overall wind-turbine performance with respect

to the ability of the blade to: (a) pass the tower with a required clearance and (b) impart the appropriate basic structural-dynamics characteristics to the HAWT-rotor and to the wind turbine, as a whole. It should be noted that an inset is provided in Fig. 10(a) in order to display the outer-skin composite-laminate lay-up used in the baseline HAWT-blade design.

A change in the base-line HAWT-blade thickness as a function of normalized distance from the blade root is displayed in Fig. 11 (the curve labeled the *Baseline Design* case). This change is a relative measure of the *flap-wise* stiffness of the blade.

In Fig. 12(a), a spatial-distribution plot of the von Mises equivalent stress over the interior box-shaped beam/spar is displayed. As mentioned earlier, the longitudinal spar is the key structural member of the blade and any compromise in its structural integrity implies an imminent loss of the HAWT-blade functionality and its structural failure. Before one can proceed with assessment of the HAWT-blade safety factor under the imposed gust-based loading conditions, one must recognize that the effective strength of the blade material may be reduced with respect to the nominally same material, but a material which is fabricated under normal material processing conditions and subjected to normal storage/handling practices.
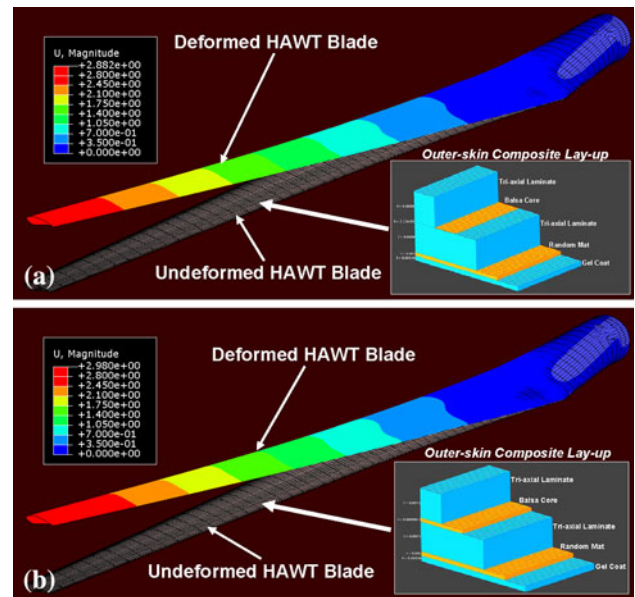

Fig. 10 Displacement magnitude distribution over the HAWT-blade outer skin caused by a 70 m/s gust: (a) the baseline case; and (b) a modified-design case

Table 1 HAWT-blade composite-laminate lay-up sequence

Layer number	Material	Thickness
Exterior skins and internal vertical shear-webs		
1	Gel coat	0.68 mm
2	Random-mat laminate	0.5 mm
3	Triaxial laminate	1.2 mm
4	Balsa core	0.005 × chord-length
5	Triaxial laminate	1.2 mm
Spar-caps		
1	Triaxial laminate	1.2 mm
2	Uniaxial laminate	1.2 mm
Continued alternating layers of 1 and 2		

Table 2 Summary of the HAWT-blade material properties

| Property	Uni	Tri	Mix	Random mat	Balsa	Gel coat	Epoxy adhesive
Axial Young's modulus, E_{xx}, GPa	31.0	24.2	27.1	9.65	2.07	3.44	2.76
Transverse Young's modulus, E_{yy}, GPa	7.59	8.97	8.35	9.65	2.07	3.44	2.76
In-plane shear modulus, G_{xy}, GPa	3.52	4.97	4.70	3.86	0.14	1.38	1.10
Possion's ratio, ν_{xy}	0.31	0.39	0.37	0.30	0.22	0.3	0.3
Fiber volume fraction, ν_f	0.40	0.40	0.40	⋯	N/A	N/A	N/A
Fiber weight fraction w_f	0.61	0.61	0.61	⋯	N/A	N/A	N/A
Density, ρ, g/cm^3	1.70	1.70	1.70	1.67	0.144	1.23	1.15
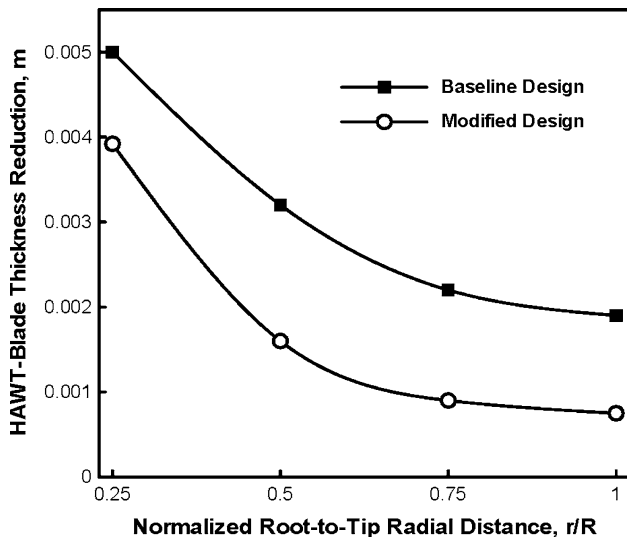
Fig. 11 Variation of the gust-induced HAWT-blade thickness for the blade designs analyzed in this work
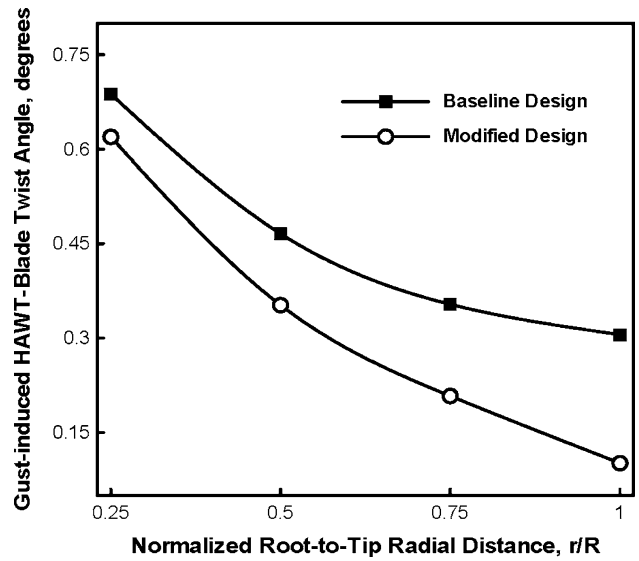

Fig. 13 Variation of the gust-induced HAWT-blade twist angle for the blade designs analyzed in this work
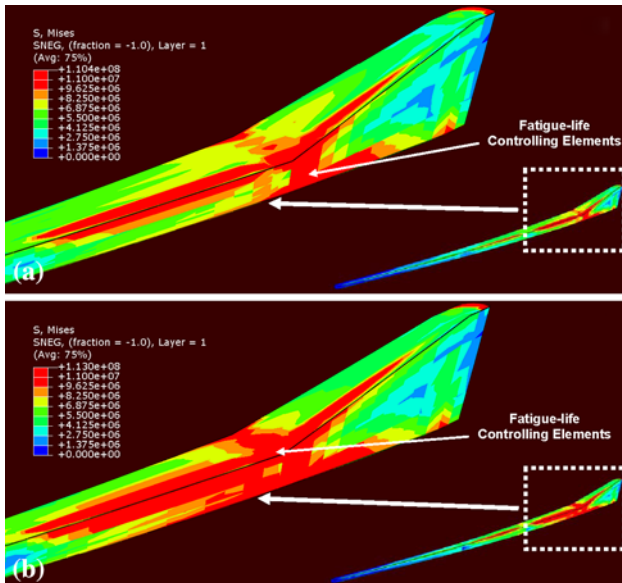

Fig. 12 Von Mises equivalent stress distribution over the HAWT interior structural members (spar-cap and shear-webs) caused by a 70 m/s gust: (a) the baseline case; and (b) a modified-design case

In comparison to the standard materials-processing practice, the material in the HAWT-blade is generally fabricated under different conditions (i.e., the material is laid-up at the time when the blade is being manufactured) and is exposed to varying temperatures, ultraviolet-radiation, humidity, salinity, and other environmental conditions (and is, hence, prone to accelerated aging/degradation). To account for all these strength-degrading effects, the IFC 61400-1 standard (Ref 7) prescribes a set of so-called *material partial safety* factors. Following the procedure described in Ref 5, the overall/cumulative material strength-reduction factor was assessed as 2.9. Hence for the prototypical 500 MPa longitudinal strength (before it is corrected using the material partial safety factors)

for the E-glass/epoxy composites used in this work, the smallest safety factor (defined as a ratio of the corrected material strength and the maximum von Mises stresses in the blade = 110.4 MPa) is estimated as (500 MPa/2.9)/110.4 MPa = 1.57.

In Fig. 13 (the curve labeled the *Baseline Design* case), a variation of the gust-induced twist angle in the blade is plotted as a function of the normalized distance from the blade root. As discussed earlier, bending-to-torsion aero-elastic effects which are responsible for the observed gust-induced blade-tip twist may play a significant role in the overall blade aerodynamic efficiency and in the passive control of the blade pitch (critical for self-protection of the blades structural integrity under excessive wind-induced loads).

3.1.2 Fatigue Life of the Baseline HAWE Blade. As mentioned earlier, the so-called *proportional loading* case was adopted in this work according to which stresses scale directly with the load magnitude and the orientation of their principal components remains unchanged with a change in the load magnitude. Hence, the stress state in the blade at any instant can be calculated by simply scaling the quasi-static stress results obtained in previous section (e.g., Fig. 12a), with the instantaneous wind-based load magnitude. However, before the fatigue life assessment procedure based on the rain flow cycle-counting algorithm, the Goodman diagram and the Miner's rule can be applied, the issue of multidimensional stress state within different components of the HAWT-blade have to be addressed. While in metallic materials compressive component(s) of the time-varying stresses are not generally harmful, composite materials (due to the potential for fiber micro-buckling) are generally quite susceptible to in-place compressive stresses. To provide a fairly conservative assessment of the baseline HAWT-blade fatigue life and take into account the effect of compressive stresses, the stress multi-axiality is handled through the use of a *signed* von Mises equivalent stress. That is, the entire stress state is assumed to be quantified by the von Mises equivalent stress to which a sign is attached consistent with the sign of the largest (by magnitude) principal stress.

As mentioned earlier, time-varying component of the wind-induced loading is modeled by the WISPER load signal. While scaling this load signal (whose values range between 1 and 64 with the level of 25 corresponding to a zero load), the WISPER mean-value was assumed to correspond to the previously computed wind mean speed of 7.6 m/s.

When the procedure outlined in Section 2.3 was applied, the fatigue life of the baseline HAWT-blade was estimated as 32.8 years. In Fig. 12(a), the elements which control the fatigue life of the blade are identified. As could have been expected, these elements are located in the airfoil/root transition region which is subjected to the highest in-service loads.

3.2 HAWT-Blade Design Modifications

The geometrical-/meshed-model generator program and the structural and fatigue-life assessment analyses developed in this work are at a level that they can be readily incorporated into a design-optimization algorithm. This will be done in our future communication, and the same design-optimization methodology as presented in our recent work (Ref 15) will be used. In this section, however, a couple of examples will be shown in order to demonstrate how few minor changes in the HAWT-blade design and composite/laminate lay-up can have significant changes to the blade response/functionality.

In Fig. 10(b), a plot is shown of the spatial distribution of displacement magnitude over the HAWT-blade surface. In comparison to the baseline HAWT-blade design (Fig. 10a), the design associated with the results displayed in Fig. 10(b) corresponds to repositioning of the right shear web from $x/c = 0.5$ to $x/c = 0.45$. Also, the composite-laminate lay-up used in the modified design case was changed by increasing the balsa core thickness by 15% relative to the baseline case. The new composite-laminate lay-up is displayed as an inset in Fig. 10(b).

A comparison of the results displayed in Fig. 10(a) and (b) shows that edge-wise stiffness of the HAWT-blade, as measured by its tip-displacement, is a fairly sensitive function of the lateral position of the right shear web.

A change in the modified-design HAWT-blade thickness as a function of the normalized distance from the blade root is displayed in Fig. 11 (the curve labeled *Modified Design*). A comparison of the results displayed in this figure for the two HAWT-blade designs analyzed indicates that repositioning of the right shear-web has measurably compromised flap-wise bending stiffness of the blade.

In Fig. 12(b), a spatial-distribution plot of the von Mises stress over the interior spar is displayed for the same HAWT-blade design as that used to generate the results displayed in Fig. 10(b). A comparison between the results displayed in Fig. 12(a) and (b) shows that the stresses are somewhat higher in the modified blade design. Consequently, the safety factor obtained using the same procedure as in the baseline case was found to be reduced from 1.57 to 1.52. Combining this finding with that made in conjunction with Fig. 10(a) and (b) and 11 suggests that there is a need for the use of design-optimization technique to identify the blade design with an optimal combination of its functional-performance measures.

The effect of a change in the shear-web/spar-cap composite-laminate lay-up relative to that used in the baseline case on the extent of bending-to-torsion coupling of the HAWT-blade is shown in Fig. 13 (the curve labeled the *Modified Design* case). In this figure, a variation of the gust-induced twist angle along

the length of the blade is displayed. A comparison of the two sets of results displayed in Fig. 13 shows that significant changes in the extent of bending-to-torsion coupling are feasible through modifications in the composite-laminate layup.

The fatigue-life assessment procedure based on the use of the rainflow cycle-counting algorithm, the Goodman diagram, and the Miner's rule yielded a fatigue life of 27.4 years for the HAWT-blade design used to generate the results displayed in Fig. 10(b) and 12(b). Again, it is clear that both the blade performance and longevity are sensitive to the blade design and that the use of design-optimization methods could be quite beneficial. This aspect of the HAWT-blade design will be addressed in our future communication.

3.3 HAWT-Blade Material Selection

In Section 2.4, it was discussed that the three most important material properties which control suitability of a given material for use in the HAWT-blade applications are the density, the Young's modulus, and the fatigue strength/life. Three related material-selection indices were also derived, and it was argued that one of them, i.e., index M_2, Eq 3, is essentially a material-property limit index which is used to screen out the materials which do not possess the sufficient level of stiffness, as quantified by their Young's modulus. Consequently, the condition $M_2 \geq 20$ GPa was applied at the onset of the present material-selection process to eliminate unacceptable materials. Then, indices M_1 and M_3 are used to carry out the HAWT-blade material selection in accordance with the procedure outlined in Section 2.4. In constructing the corresponding material-selection charts various open-literature material-data sources were consulted. The Young's modulus data used pertain to the mean in-plane value of this quantity. The results of the material-selection procedure carried out in this work are summarized in Fig. 14(a) to (c). It should be noted that, for clarity, materials appearing in Fig. 14(a) to (c) are labeled using numbers and a legend is provided in Fig. 14(d) for the number labels used.

In Fig. 14(a), the Young's modulus versus density data are compiled for a number of thermosetting-polymer matrix composites. A log-log plot was used in Fig. 14(a) and three lines with a constant slope were drawn in accordance with the definition of the first material-selection index, M_1 (Eq 2). The three guidelines (with a slope of 2.0) are associated with the M_1-levels of 10,500, 22,500, and 40,000 GPa$^{0.5}$/(kg/m^3) with the larger M_1 value causing the guideline to be shifted upward. Also, a 20 GPa dashed guideline is displayed in Fig. 14(a) in order to denote the previously established lower-bound for the Young's modulus of the candidate materials for use in the HAWT-blade applications. With respect to the M_1 material-selection index alone, the optimal materials are those located above the topmost guideline.

In Fig. 14(b), a linear-linear plot is shown of the data pertaining to the endurance limit (*x*-axis) and the toughness (*y*-axis) for the same set of materials as that used in Fig. 14(a). Three solid guidelines are also shown in Fig. 14(b), and they correspond to the M_3-levels of 1, 7, and 13 MPa^2 m. Again, with respect to the M_3 material-selection index alone, the optimal materials are those located above the topmost guideline.

Since different material are identified as optimal if material selection is based on the use of a single index (M_1 or M_3, Fig. 14a and b), a procedure was developed here which takes
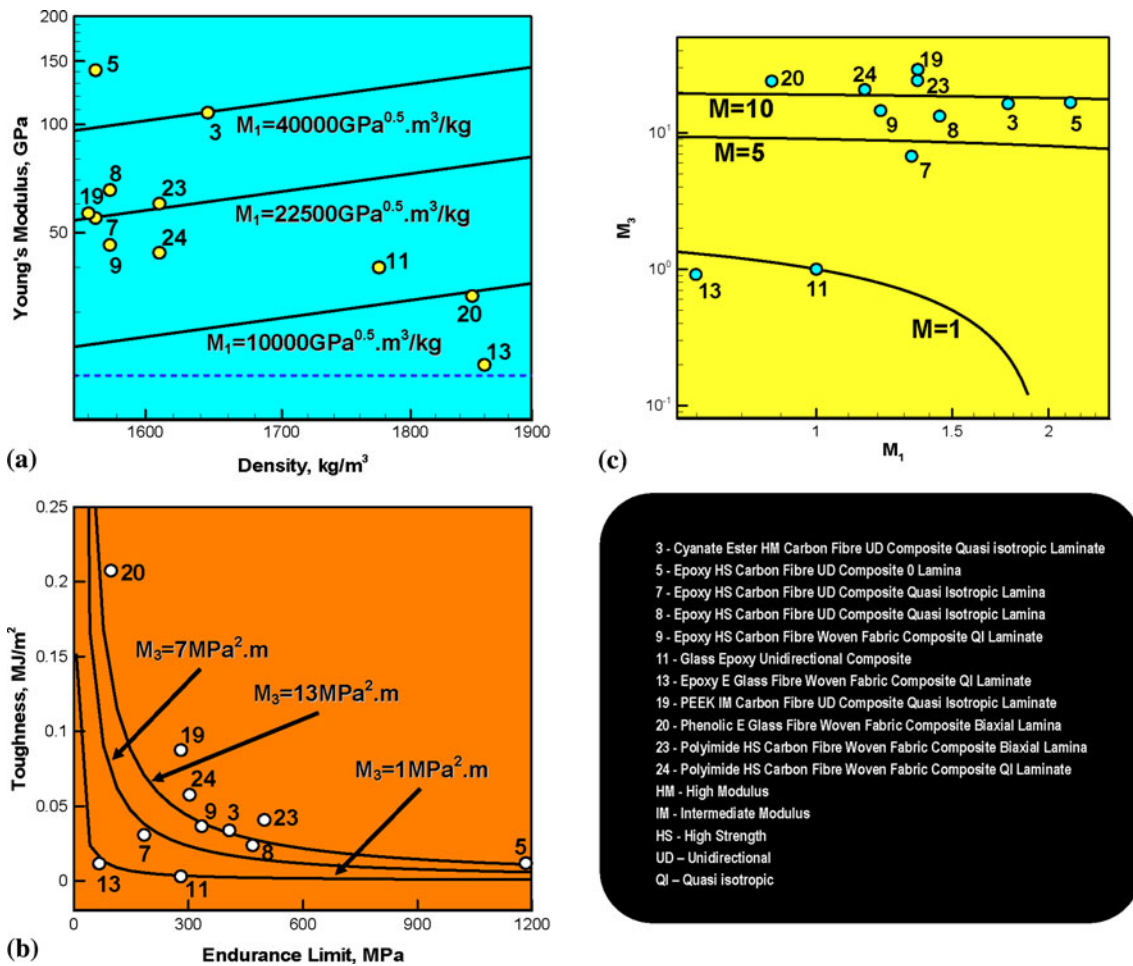
Fig. 14 Material-property charts used in the HAWT-blade material-selection process. Please see text for details

into account both of these material indices in the HAWT-blade material-selection process. A linear-linear plot of M_3 versus M_1 material-selection indices (normalized by the values of these two indices in a commonly used HAWT-blade material, i.e., an E-glass uni-directionally reinforced epoxy-matrix composite) is shown in Fig. 14(c). The three solid lines displayed in Fig. 14(c) correspond to the values of 2, 5, and 10 for a combined material-selection index, M, defined as:

$$M = wM_1 + (1 - w)M_3, \qquad \text{(Eq 5)}$$

where the weighting factor w for the material-selection index M_1 is set 0.5, making the weighting factor for the mutual selection index M_3 also equal 1.0-0.5 = 0.5.

Simple examination of the results displayed in Fig. 14(c) reveals that, for the most part, carbon-fiber reinforced PEEK-(Poly-ether-ether-ketone) or polyimide-matrix composites are favored. In the case of E-glass fiber reinforced composites, a phenolic matrix appears to be preferred over the traditionally used epoxy or poly-ester. The main reason for the carbon fibers outperforming the E-glass fibers is their higher density-normalized stiffness, while the emergence of the phenolic polymers appears to be related to higher toughness levels imparted to the composite material by this polymeric matrix. The main reason for the currently preferred HAWT-blade material, i.e., E-glass fiber reinforced epoxy-matrix composites,

is the relatively low material cost combined with the overall good structural/fatigue-life performance.

It should be noted that the material-selection procedure employed in this work is based on the use of stereotypical material properties of the common thermosetting-polymer matrix composite plies/laminae reinforced with either uni-directional or cross-woven fiber mats. Consequently, the procedure does not include the full effect of composite-laminate architecture. That is, properties of the composite laminates are derived not only from those of the associated laminae, but also can be tailored over relatively large range by varying plies thickness and orientation, stacking sequence as well as by hybridization of the laminate. Laminate hybridization can be carried out on the ply scale (by combining fibers of different types, e.g., by combining glass and carbon fibers within the single laminae) or on the laminate scale (by stacking plies with different fiber reinforcements, e.g., by alternate stacking of the glass-fiber reinforced plies and the carbon-fiber reinforced plies). It should be noted that ply-level hybridized laminae can be readily included in the present material-selection procedure once the appropriate material properties become available. On the other hand, the effect of laminate-level hybridization can be readily included through the ply-stacking optimization procedure mentioned in Section 3.2.

4. Summary and Conclusions

Based on the results obtained in this work, the following main summary remarks and conclusions can be drawn:

1. A fully parameterized computer program has been developed for automated generation of the geometrical and finite-element meshed models of the HAWT-blades. The program enables the specification of the basic blade geometrical and structural parameters (e.g., airfoil shape, size and lateral location of the longitudinal spar/beam, thickness of the adhesive layers joining the beam to the external blade skins, etc.) as well as the basic and locally different composite-laminate architecture and lay-up sequence.
2. Fairly realistic, yet generic wind-based (sustained and time-varying) loading conditions are compiled and applied to a stereotypical 1 MW HAWT-blade in order to assess its structural response as well as to assess its longevity.
3. A preliminary parameter variation study was conducted which revealed that further improvements in the HAWT-blade performance are possible with targeted changes in the blade geometry and the composite-laminate lay-up.
4. A simple HAWT-blade material-selection procedure was developed which combines weighted contributions of the material indices pertaining to the blade performance and longevity. The results revealed that, as expected, from the performance point of view carbon-fiber reinforced composites are preferred over the traditionally used E-glass fibers reinforced composites and that epoxy may not be best choice for the composite-material matrix.

References

1. "20% Wind Energy by 2030, Increasing Wind Energy's Contribution to U.S. Electricity Supply," DOE/GO-102008-2567, July 2008, http://www.osti.gov/bridge
2. T. Burton, D. Sharpe, N. Jenkins, and E. Bossanyi, *Wind Energy Handbook*, Wiley, USA, 2001
3. M. Selig, "UIUC Airfoil Coordinates Database—Version 2.0," http://www.ae.uiuc.edu/mselig/ads/coord_database.html, 2006
4. MATLAB, *The Language of Technical Computing*, 7th ed., The MathWorks Inc., MA, 2006
5. D.A. Griffin, *WindPact Turbine Design Scaling Studies Technical Area-1-Composite Blades for 80- to 120-Meter Rotor*, NREL, Washington, 2001
6. M. Hepperle, *JavaFoil Users Manual*, http://www.mh-aerotools.de/airfoils/javafoil.htm, 2005
7. IEC-61400-3 (2009-02) Wind Turbines—Part 3: Design Requirements for Offshore Wind Turbines Maintenance Result Date, p 201
8. A.A. Ten Have, "WISPER and WISPERX: Final Definition of Two Standardized Fatigue LoadingSequences for Wind Turbine Blades," NLR-TP-91476U, National Aerospace Laboratory NLR, Amsterdam, the Netherlands, 1992
9. ABAQUS/Standard Version 6.8-1, *User Documentation, Dassault Systemes*, Providence, RI, 2008
10. M. Matsuiski and T. Endo, *Fatigue of Metals Subjected to Varying Stress*, Japan Soc. Mech. Eng., Fukuoka, 1969
11. J. Goodman, *Mechanics Applied to Engineering*, Longman, Green & Co, London, 1899
12. M.A. Miner, Cumulative Damage in Fatigue, *J. Appl. Mech.*, 1945, **12**, p A159-A164
13. M.F. Ashby, *Materials Selection in Mechanical Design*, 3rd ed., Elsevier Butterworth Heinemann, UK, 2005
14. D.M. Somers, *The S816, S817 and S818 Airfoils*, NREL, Pennsylvania, 1992
15. M. Grujicic, G. Arakere, W.C. Bell, H. Marvi, H.V. Yalavarthy, B. Pandurangan, I. Haque, and G.M. Fadel, Reliability-Based Design Optimization for Durability of Ground-Vehicle Suspension-System Components, *J. Mater. Eng. Perform.*, accepted for publication, April 2009